A surface morphology-based inference method for the cell wall elasticity profile in tip-growing cells

Rholee Xu[1], Luis Vidali[1,2*], Min Wu[1,3*],

1 Bioinformatics and Computational Biology Program, Worcester Polytechnic Institute, Worcester, MA, USA
2 Department of Biology and Biotechnology, Worcester Polytechnic Institute, Worcester, MA, USA
3 Department of Mathematical Sciences, Worcester Polytechnic Institute, Worcester, MA, USA

* lvidali@wpi.edu, englier@gmail.com

Abstract

Plant cell morphology and growth are essential for plant development and adaptation, in particular the cell wall material deposition and rearrangement. As the wall is extended due to turgor pressure, the wall mechanical response, specifically the wall's elastic properties, are not well understood. In this study, we introduce a new surface morphology-based method to measure the elasticity of the cell wall in tip-growing cells. Previous work is based on the wall meridional outline on the assumption the cell is axisymmetric, an idea that does not align well with the reality of the cells. Instead, we developed a way to triangulate the surface of the cell using marker point locations that could be achieved experimentally with fluorescent labeling. After measuring the elastic stretch and curvatures from our triangulation, a mechanical model is used to measure the tensions and surface bulk modulus distribution. We simulated moss tip cells from experimental *Physcomitrium patens* plants to challenge the method with noise estimated from experiments. We discovered that increasing the discretization of the triangulation improved robustness against noise. With multiple cell sampling, we found that around 10 cells were sufficient to recover the elasticity distribution with noise, but only when the elastic stretches were high enough at the tip. With low elastic stretch at the tip, the appearance of non-physical modulus values led to underestimated inference values there, causing false-positive gradient results. This compelled us to study a range of cases, leading us to a dimensionless global phase map showing areas of good inference. This technique will open the field to more comprehensive measurements of tip cell elasticity, providing a key step in understanding tip cell growth and morphogenesis.

Author summary

Tip-growing cells can be characterized by their fast growth concentrated at the cell's apex. Their growth and morphogenesis are tightly regulated processes involving cell wall addition and rearrangement, which aim to reduce the wall stress originating from the cell's internal turgor pressure. We simplify this cell growth system by first studying the cell wall's elastic properties that are present without active growth. We use a surface triangulation method derived from marker point tracking to measure the spatial elasticity along the tip cell. In this work, we present a parameter sensitivity study of

this method on synthetic cells that cover a tapered and round cell morphology. Our results suggest that this inference method can reliably measure a cell wall elasticity gradient under combined geometric and mechanical conditions that create large enough elastic strain at the tip.

Introduction

The dynamic ability of cell walls to consistently add and rearrange wall material while extending is often understated, as we commonly view the wall as a rigid material. The wall itself defines the morphology of walled cells and provides protection, but must sustain internal pressures up to 1000 times higher than in animal cells [1–3]. Hence, the morphogenesis and growth of walled cells strongly depend on the mechanics of the cell wall, especially how those mechanics differ in particular areas along the cell surface. Tip-growing cells are an ideal system for studying these spatial mechanical differences because of their simple morphology and concentrated surface expansion at the tip of the cell. Given that this feature is conserved across many eukarytotic species, it is likely to have been selected to support fast linear growth [4]. In plant species, tip-growing cells such as root hairs are essential for acquiring water and nutrients [5], and pollen tubes are needed for fertilization [6]. Additionally, moss protonema like in the model organism *Physcomitrium patens*, utilize tip growth for fast surface area expansion [7]. Outside of plants, tip-growing cells like fungal hyphae or water molds may serve other functions such as invasive growth, but with a similar underlying goal of efficient expansion [4, 8, 9]. Understanding how tip-growing cells can maintain stable cell wall growth against their strong internal turgor pressure is essential to the field of plant growth and morphology.

The scale of single tip-growing cells make it difficult to measure wall mechanics, especially at discrete spatial locations. These measurements have been more easily accomplished at larger scales, for instance in plant tissues. The physical clamping and stretching of onion epidermal cells is one such example [10–12]. In tip-growing cells, the use of micro-indentation has been a common tool used to measure local mechanical differences in pollen tubes [13–15]. Due to the geometrical orientation of the probing, the measurement may not provide a direct measurement of the mechanics relevant to wall expansion. Instead of experiments, many mechanical models have been developed since the Lockhart model, which described wall extension as a function of wall extensibility, regulated by turgor pressure [16]. Subsequent tip growth models expanded upon this idea by adding a spatial component, while taking advantage of the tip cell axial symmetry [9, 17–22]. The models note that a steep gradient of mechanical properties moving away from the tip is needed to produce efficient cell wall extension that matches observed growth and realistic morphologies. An alternative to Lockhart is the idea that the wall growth comes from the combination of two actions, the first of which is the reversible elastic deformation defining the change from an unturgid to a turgid configuration [23, 24]. The second action involved is the irreversible wall expansion, coming from wall biochemical processes. The connection between these two processes was explored in yeast, where they first found cell wall elastic changes of up to 20% when the turgor pressure was removed [23]. The morphogenesis was then modeled with the elastic component, and it was found that when the irreversible growth was closely proportional to the elasticity, there was good agreement between the simulated wall extension and experiments [23, 25, 26]. More recently in filamentous fungi, similar deformation experiments were used to estimate the elastic properties at the tip and shank [27]. Importantly, the results showed a gradient of properties within one order of magnitude. However, without the tracking of material points on the wall, the measurement assumes that the wall strain has the same trend as the wall curvature, which was not tested. To truly support the applicability of the second type of model in

tip-growing cells, a more detailed measurement of the elastic properties at the region of transition from the side to the tip is needed.

The feasibility of an axisymmetric marker point inference scheme on the wall outline was demonstrated in [28] and [29] to track the wall tensions and elastic moduli, respectively. In experiments, such marker point tracking can come from fluorescent beads (Fig 1A) or quantum dots that can be adhered to the cell wall surface [23]. However, instead of relying on the assumed cell symmetry for the initial measurement, we developed a surface morphology-based method pipeline to measure the deformation on the wall surface. The method will compute the curvatures and surface deformations, and then reduce them into the elastic moduli in the axisymmetric wall outline model. In particular, we generated simulated cells from experimental *P. patens* cell wall outlines to validate the method with varying levels of noise estimated from experiments. Our results suggest that, when there is noise, the elasticity profile can be recovered by using a coarser discretization of triangles and multiple cell samples.

Methods

Cell wall surface tracking of elastic deformation and curvature

Automated triangulation of cell wall surface marker points: To triangulate the surface, we first select a subset of marker points around the cell surface (Fig 1A, C). In experiments, the marker points can come from the adhesion of fluorescent beads or quantum dots, for instance [9, 20, 23]. To ensure the accuracy of the marker points, they should be localized to a sub-pixel resolution, then tracked between the turgid to unturgid configuration. The unturgid state can be obtained by removing turgor pressure with an osmoticum change [23, 29] (Fig 1A bottom) or laser ablation [27, 30]. To standardize our triangulation process when given a subset of marker points, we devised an automated method by Delaunay triangulation (Fig 1D). We employ the `delaunay` function in Matlab [31]. The function will not automatically triangulate on the curved cell wall surface. To utilize the planar Delaunay triangulation, we apply a stereographic-like projection to the points onto an x-y-plane above the cell (Fig 1D, i-iii). Due to the shape transition of the cell, the marker points at the tip are projected from a single point located at the center of that area, while in the pipe region each marker point is projected from a point on a center line through the cell (Fig 1D, ii). After projection, we apply the `delaunay` function to obtain our connectivity map (Fig 1D, iv). The same connectivity map is applied to the original marker points to obtain the final triangulated surface (Fig 1E). Given the one-to-one correspondence of marker points in the turgid and unturgid configuration, the same triangulation is used for the unturgid cell. With synthetic marker points, the triangulation size can be adjusted by changing the initial number of random marker points chosen (N_Δ), and the distance boundary used to filter points too close to each another (d_Δ). For a unique triangulation, the mean triangle area, $\bar{\Delta}_A$ can be non-dimensionalized using the cell radius $\bar{L}$: $\bar{\Delta}_A/\bar{L}^2$.

Computation of the elastic deformations from the wall surface: In finite strain theory, the deformation gradient relates the reference and current configuration of a given region [32]. In our case, we use the deformation gradient, F, to connect the surface patches in the turgid and unturgid configuration (Fig 2A). Our mapping of the surface patches is done between each triangle on the turgid and unturgid triangulations. The pair of triangles are defined by $\mathbf{B} = [\vec{v}_1^b, \vec{v}_2^b, \hat{n}^b]$ and $\mathbf{A} = [\vec{v}_1^a, \vec{v}_2^a, \hat{n}^a]$, respectively. Here, $\vec{v}_1$ and $\vec{v}_2$ are the vectors defining any two sides of the triangle, and $\hat{n}$ is the triangle's normal vector (Fig 2B). The polar decomposition of the deformation gradient $\mathbf{F}$ is: $\mathbf{F} = \lambda_1 \hat{x}_1^b \otimes \hat{x}_1^a + \lambda_2 \hat{x}_2^b \otimes \hat{x}_2^a + \hat{n}^b \otimes \hat{n}^a$, where λ_1 and λ_2 are the principal stretch

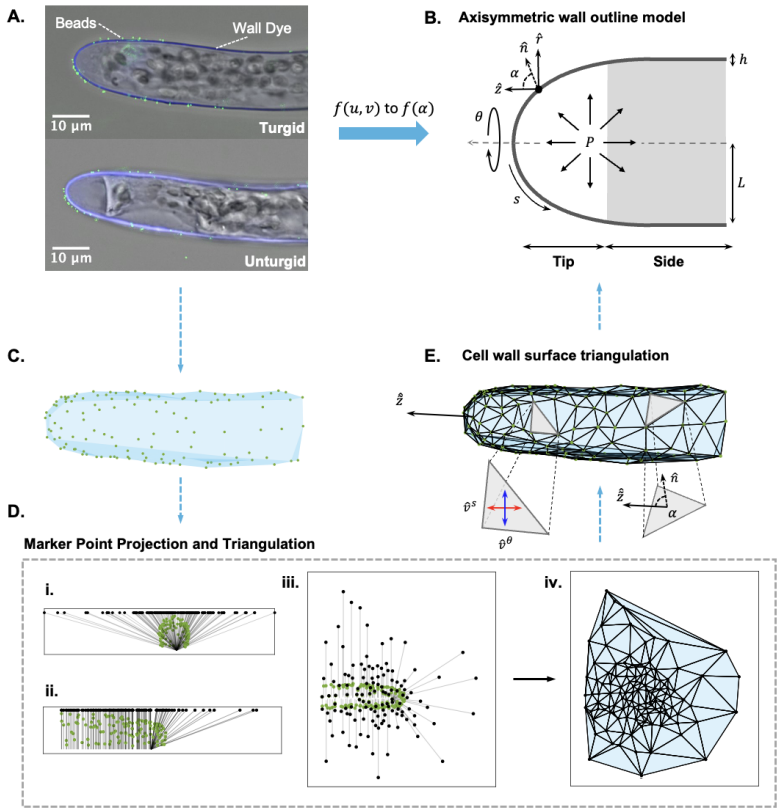

Fig 1. Marker point triangulation scheme connects the cell wall surface to the axisymmetric wall outline. A. *P. patens* tip cell labeled with calcofluor white and adhered with fluorescent beads (Thermofisher). The unturgid cell (below) comes from the plasmolysis of the turgid cell (above) after the addition of a 15% mannitol solution. **B.** Standard thin-shell axisymmetric outline model of a tip growing cell. Non-dimensional parameters include the turgor pressure (P), cell wall thickness (h), cell radius (L), and the circumferential (θ) and meridional (s) coordinates (see Methods). Each wall point has a local angle ($\alpha = \cos^{-1}(\hat{n} \cdot \hat{z})$) between the outward normal ($\hat{n}$) and long axis ($\hat{z}$). The gray area denotes our demarcation of the cell side from the cell tip area (which covers a range of $80 \leq \alpha \leq 90$). **C.** Translation of the fluorescent bead covered surface into Matlab. **D.** Automated bead projection and triangulation process. **(i-iii)** Bead projection onto x-y-plane from three views: **(i)** front, **(ii)** side, and **(iii)** top. **(iv)** Automated triangulation in the 2D plane. **E.** Final triangulation on the 3D cell. Different components include the new optimized long axis, $\hat{\tilde{z}}$, the calculation of α on each triangle (S1 Fig), and the optimized circumferential and meridional directions, $\hat{v}_s$ and $\hat{v}_\theta$, respectively (see Methods).

.

ratios in the local tangent plane. Notice that $\hat{n}^b \otimes \hat{n}^a$ describes the rotation of the local tangents. The right and left Cauchy-Green tensors are $\mathbf{F}^T\mathbf{F}$ and $\mathbf{F}\mathbf{F}^T$, respectively [33]. The square root of the non-unity eigenvalues of these matrices gives the values of λ_1 and λ_2. The eigenvectors of $\mathbf{F}^T\mathbf{F}$ that are not $\hat{n}^a$, describe the principal directions in the unturgid configuration, $\hat{x}_1^a, \hat{x}_2^a$. The eigenvectors of $\mathbf{F}^T\mathbf{F}$ that are not $\hat{n}^b$, describe them in the turgid configuration $\hat{x}_1^b, \hat{x}_2^b$. In summary, the decomposition of $\mathbf{F}$ shows that $\mathbf{F}$ is simply a way to transform any vector on the tangent plane of the unturgid patch to the turgid patch, including the unit normal vectors (Fig 2B). Conversely, we can use

$\mathbf{F}^{-1} = \frac{1}{\lambda_1}\hat{x}_1^a \otimes \hat{x}_1^b + \frac{1}{\lambda_2}\hat{x}_2^a \otimes \hat{x}_2^b + \hat{n}^a \otimes \hat{n}^b$ to transform a vector on the turgid patch to the unturgid patch. The calculation of F in practice can follow: $\mathbf{F} \cdot \mathbf{A} = \mathbf{B}$. Therefore:

$$\mathbf{F} = \mathbf{B} \cdot \mathbf{A}^{-1} \tag{1}$$

The linear map $\mathbf{F}$ and the principal directions, $\hat{x}_1^b, \hat{x}_2^b$, are used as a local basis to find the optimized circumferential and meridional directions in a later section.

Since $\mathbf{A}$ and $\mathbf{B}$ are constructed from the coordinates of triangle vertices, we analyzed how perturbations on the triangle vertices are propagated to the calculation of $\mathbf{F}$ (See Section 1.3 in S1 Text). In particular, we derived a formula $\frac{\|\delta\mathbf{F}\|_2}{\|\mathbf{F}\|_2} \leq \Gamma|\varepsilon|$, where $\frac{\|\delta\mathbf{F}\|_2}{\|\mathbf{F}\|_2}$ is the relative error, and $\Gamma|\varepsilon|$ is a function of geometric parameters related to the triangle. The $|\varepsilon|$ term sets the scale for some perturbation on the vertices (S1 Text). Given that Γ describes the sensitivity of a triangle to noise, we used the distribution of triangle Γ values to set a threshold to remove more sensitive triangles. We found that this effectively retained triangles with a more compact shape.

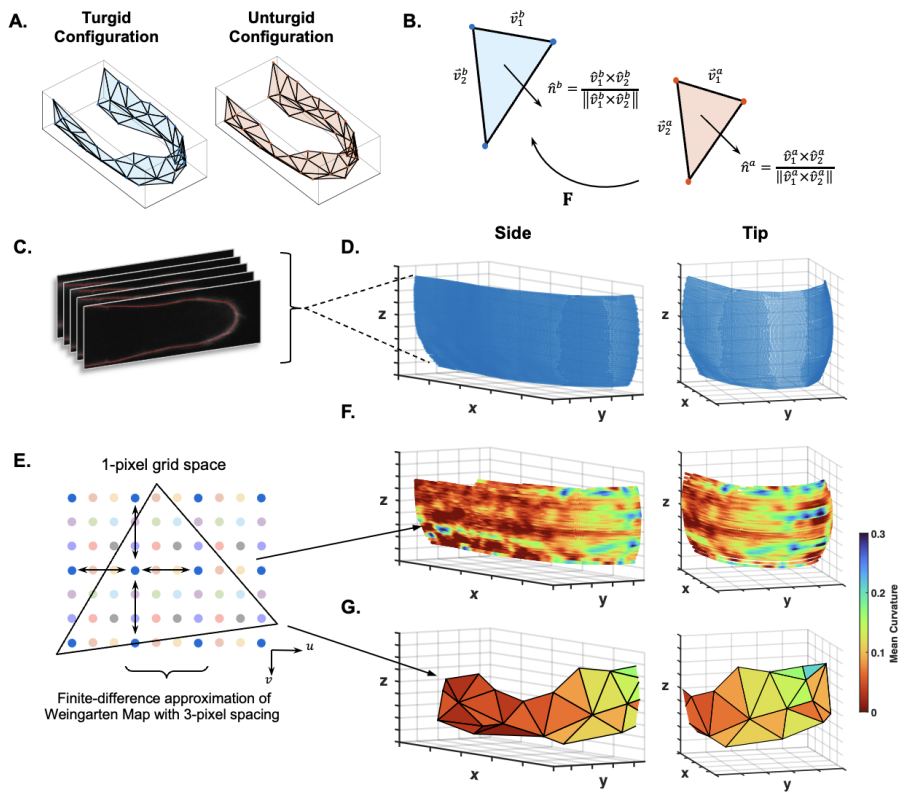

Fig 2. Elastic stretch and curvature calculation on the triangulated cell wall surface. A. Turgid and unturgid triangulations (following Fig 1). **B.** The linear map $\mathbf{F}$ describes the deformation of the unturgid triangle (red) to the turgid triangle (blue) through each triangle's side vectors ($\vec{v}$) and normal vectors ($\hat{n}$). **C.** Collection of Z-stack images collated to reconstruct cell wall surface. **D.** Raw data of an experimental cell surface, shown from the side and tip. **E.** Demonstration of the finite-difference approximation with a 3-pixel spacing. Shifting covers the entire 1-pixel grid space. **F.** Mean curvature values on each wall point associated to each triangle are averaged (**G**). See S2 Fig for more details.

Computation of the curvatures from the wall surface: The standard calculation of principal curvatures in the outline model and previous works is denoted by:

$\bar{\kappa}_s = d\alpha/ds$ and $\bar{\kappa}_\theta = \sin\alpha/r$ [17,34,35]. On the wall surface, the s and r parameters are hard to define even in the optimal sense. Thus, we obtain the curvature tensors from the surface data, and then $\bar{\kappa}_s$ and $\bar{\kappa}_\theta$ along the locally optimized meridional and circumferential directions. We start by utilizing any available cell wall outline data (Fig 2C). Then we parameterize the surface regions into a grid, $X(u,v) = (x,y,z)$, using the Matlab functions `meshgrid` and `griddata` [36,37], so that we can use finite differences to calculate the local tangent vectors. The grid parametrization can be (x,y), (x,z), or (y,z) depending on the cell surface orientation (Fig 2D). The first function, `meshgrid`, takes in the coordinate range of the parameterized surface along with a specified pixel spacing, which we will discuss at the end of the section. This then returns the corresponding uniform 2D grid coordinates in the parametric space (Fig 2E).

The second function, `griddata` with option "`cubic`", will interpolate the original outline at the query points defined by the 2D grid to give us $X(u,v)$ where u,v live on the grid (Fig 2E, F). $X(u,v)$ is then used to calculate the local Weingarten Map [38]:

$$W = \begin{bmatrix} E & F \\ F & G \end{bmatrix}^{-1} \begin{bmatrix} L & M \\ M & N \end{bmatrix} \tag{2}$$

with the first and second fundamental coefficients,

$$\begin{aligned} E &= X_u \cdot X_u \\ F &= X_u \cdot X_v \\ G &= X_v \cdot X_v \end{aligned} \tag{3} \qquad \begin{aligned} L &= X_{uu} \cdot \hat{n} \\ M &= X_{uv} \cdot \hat{n} \\ N &= X_{uu} \cdot \hat{n} \end{aligned} \tag{4}$$

where $\hat{n}$ is the unit normal on each point and $X_\square = [x_\square, y_\square, z_\square]$. The subscripts, $\square$, are the partial derivatives of X in the u and v directions (Fig 2E, u,v arrows), and those partial derivatives are approximated by the `gradient` function in Matlab [39]. The eigenvalues of W give the principal curvatures, $\bar{\kappa}_1(u,v)$ and $\bar{\kappa}_2(u,v)$ in the parameterized space. Say $\begin{bmatrix} u_1' \\ v_1' \end{bmatrix}, \begin{bmatrix} u_2' \\ v_2' \end{bmatrix}$ are the eigenvectors of W corresponding to the eigenvalues. Then the principal directions in 3D are: $\vec{\alpha}_1 = u_1' X_u + v_1' X_v$ and $\vec{\alpha}_1 = u_2' X_u + v_2' X_v$ followed by normalization.

The high resolution of the image raw data introduces local waviness and distortion of the cell wall not relevant to the curvature at the cell size level (S2 FigA). Additionally, we observed that the finite difference method is sensitive at the edges of the grid. We adopted a border removal process to effectively remove outliers along the edges. To filter out the local waviness, we found that increasing the pixel spacing used to create $X(u,v)$ could smooth the results (S2 FigA, S2 FigB). As the spacing increases, the border removal process will naturally remove larger chunks of data. Although these areas can be recovered with additional parameterizations, for simplicity we have opted to use a spacing of 3 pixels (Fig 2E). Our final principal curvature values include repeating the entire process by shifting the interpolated mesh n times, depending on the spacing. This allows us to cover the whole 1-pixel grid space (Fig 2E, 2F).

Cell wall mechanics model

Axisymmetric cell wall outline model: To model the mechanics of the cell on the wall outline, we describe the wall as a thin pressurized shell revolved around an axis of symmetry (Fig 1B). In the axisymmetric system, the wall properties can be defined on two orthogonal directions along the circumferential (θ) and meridional (s) coordinates. The cell wall stresses in the circumferential and meridional directions ($\bar{\tilde{\sigma}}_\theta, \bar{\tilde{\sigma}}_s$) must balance the force in the system coming from the internal turgor pressure, $\bar{P}$. This results in the Young-Laplace Law which can be used to infer the wall tensions from the

wall curvatures $(\bar{\kappa}_\theta, \bar{\kappa}_s)$ [17,18,28,35].

$$\bar{\sigma}_s = \bar{P}/(2\bar{\kappa}_\theta) \tag{5}$$

$$\bar{\sigma}_\theta = \bar{P}/(2\bar{\kappa}_\theta) \times (2 - \bar{\kappa}_s/\bar{\kappa}_\theta) \tag{6}$$

Here, the wall tensions, $\bar{\sigma}_s$ and $\bar{\sigma}_\theta$, are equal to in-plane wall stresses multiplied by the cell wall thickness h: $\bar{\sigma}_\theta = \bar{\bar{\sigma}}_\theta \times h$ and $\bar{\sigma}_s = \bar{\bar{\sigma}}_s \times h$. To describe the cell wall mechanics, we assume that the tensions are sustained by the cell wall elasticity.

While many cell walls may present anisotropic material property due to the fiber alignments [2], there are cell walls such as moss [40] that have fibers aligning with the wall surface, and distribute without preferred directions within the local plane. This can justify a 2D isotropic material [17]. For simplicity, we assume the 2D nonlinear Hookean constitutive law relates the tensions with the elastic stretch ratios through two material properties, the surface bulk and shear modulus, $\bar{K}_h$ and $\bar{\mu}_h$, respectively [28,29].

$$\bar{\sigma}_s = \frac{1}{2}\bar{\mu}_h(\frac{1}{\lambda_\theta^2} - \frac{1}{\lambda_s^2}) + \bar{K}_h(\lambda_s\lambda_\theta - 1) \tag{7}$$

$$\sigma_\theta = \frac{1}{2}\bar{\mu}_h(\frac{1}{\lambda_s^2} - \frac{1}{\lambda_\theta^2}) + \bar{K}_h(\lambda_s\lambda_\theta - 1) \tag{8}$$

The elastic stretch ratios, λ_s and λ_θ, describe the change from the unturgid to turgid configuration. These can be related to the elastic strains, ϵ as follows: $\epsilon_s = \lambda_s - 1$ and $\epsilon_\theta = \lambda_\theta - 1$. When the elastic strains are small, $|\epsilon| << 1$, we observe that our nonlinear constitutive law is equivalent to a linear elastic law [24]. In this circumstance, the surface bulk and shear modulus can be connected to the surface Young's modulus and Poisson's ratio through: $\bar{\mu}_h = \frac{\bar{E}_h}{2(1+\nu)}$ and $\bar{K}_h = \frac{\bar{E}_h}{2(1-\nu)}$. The surface moduli can all be related to the 3D moduli through h: $\bar{E}_h = \bar{E} \times h$, $\bar{K}_h = \bar{K} \times h$ and $\bar{\mu}_h = \bar{\mu} \times h$. Subsequently, $\bar{K}_h$ and $\bar{\mu}_h$ can be be measured by rearranging Eqs 7 and 8:

$$\bar{K}_h = \frac{\bar{\sigma}_s + \bar{\sigma}_\theta}{2(\lambda_s\lambda_\theta - 1)} \tag{9}$$

$$\bar{\mu}_h = \frac{\bar{\sigma}_s - \bar{\sigma}_\theta}{1/\lambda_\theta^2 - 1/\lambda_s^2} \tag{10}$$

In the results, we will present the non-dimensionalized variables: $\kappa_{s,\theta} \to \bar{\kappa}_{s,\theta}\bar{L}$, $\sigma_{s,\theta} \to \bar{\sigma}_{s,\theta}/\bar{P}\bar{L}$, and $K_h \to \bar{K}_h/\bar{P}\bar{L}$.

Instability of the bulk and shear modulus against small perturbations: Previously in [29], the effect of perturbations on the tensions and stretches on $\bar{K}_h$ and $\bar{\mu}_h$ was analyzed. In essence, we can observe that the inference of $\bar{K}_h$ will suffer when the denominator approaches 0, which is when $\lambda_s\lambda_\theta$ approaches 1 (Eq 9). When $\lambda_s\lambda_\theta < 1$, negative $\bar{K}_h$ values will appear. Since these values are non-physical, we remove calculations with negative $\bar{K}_h$ from all of our results. On the other hand, the inference of $\bar{\mu}_h$ is unstable when $\sigma_s \approx \sigma_\theta$ and/or $\lambda_s \approx \lambda_\theta$ (Eq 10). Due to the isotropic nature of the tip cell, this will always occur at the tip. Even in the purely axisymmetric case, we have already observed that the inference of $\bar{\mu}_h$ is sensitive at the tip [29]. For those reasons, this paper will focus on the robustness of inferring just the bulk modulus. Similar to other work, we will only measure one elastic property and make a generalization of $\bar{\mu}_h$ to support our analysis [4,27].

Elastic moduli inputs and forward model determine turgid cell shape: The computational membrane deformation model established in [29] can be employed to generate the turgid configuration given the unturgid configuration and specified

distribution of elastic moduli. The range of $\bar{K}_h$ and $\bar{\mu}_h$ starting values were based on preliminary results of λ_θ at the cell side, ranging between $1.05 \leq \lambda_\theta \leq 1.25$ [29].

We created three cases of bulk modulus distributions as a function of the cell length, z. These include nonlinearly decreasing and linearly decreasing towards the cell tip z_{tip}, and a constant distribution. The constant case is simply:

$$\bar{K}_h(z) \equiv \bar{K}_{side} = \bar{K}_{tip} \tag{11}$$

The linear case is:

$$\bar{K}_h(z) = \begin{cases} \bar{K}_{side} & 0 \leq z < z_1 \\ \bar{K}_{tip} + (\frac{1}{z_{tip}-z_1})(\bar{K}_{tip} - \bar{K}_{side})(z - z_{tip}) & z \geq z_1 \end{cases} \tag{12}$$

and the nonlinear distribution is given by:

$$\bar{K}_h(z) = \frac{1}{2}(\bar{K}_{side} - \bar{K}_{tip})(1 - \tanh(\frac{z - z_2}{w})) + \bar{K}_{tip} \tag{13}$$

In both cases, z_1 and z_2 specify where the linear and nonlinear cases begin to decrease towards the tip, respectively. In our case, we used $z_{tip} = 4$, $z_1 = 2$, $z_2 = 3$, and $w = 0.2$ (see Fig 3Bi for cell orientation and z_{tip}). In the results, the distributions are converted to the local angle α. The steepness of the gradient $\bar{K}_{side}/\bar{K}_{tip}$ was also chosen to reflect the proper elastic stretch ratios and wall outlines. We found that, unlike previously reported [17, 19], a gradient too large would cause non-monotone outlines (see also [28]). Although these morphologies may exist, for the purposes of this analysis and our estimates of *P. patens* tip cell morphologies, the gradient of $\bar{K}_h$ will be limited to $\bar{K}_{side}/\bar{K}_{tip} \leq 4.67$ throughout all study cases.

We found that the trend of $\bar{\mu}_h$ in comparison to $\bar{K}_h$ had no significant effects on the cell shape (S4 Fig). Despite effects on the elastic stretch ratios, since we do not infer $\bar{\mu}_h$ in this paper, we choose one of the three cases. Here, we have chosen $\bar{\mu}_{side} = \bar{K}_{side} - 2$ and $\frac{\bar{K}_{side}}{\bar{K}_{tip}} = \frac{\bar{\mu}_{side}}{\bar{\mu}_{tip}}$, meaning $\bar{\mu}_{tip} = \frac{\bar{\mu}_{side}\bar{K}_{tip}}{\bar{K}_{side}}$. This ensures a consistent ratio of $\bar{K}_h$ and $\bar{\mu}_h$ across the cell, leading to a constant Poisson's ratio. With $\bar{\mu}_{side}$ and $\bar{\mu}_{tip}$, the distribution of $\bar{\mu}_h$ is given the same distribution as $\bar{K}_h$, calculated by Eqs 11, 12, or 13.

Conversion of variables from the wall surface to the outline model

Computation of surface parameters in the circumferential and meridional directions: To use the axisymmetric outline model to measure the wall mechanics, we must find the circumferential and meridional directions in a more generalized setting on each triangulated surface patch (Fig 1B θ and s, to Fig 1E blue and red arrows). We first define a vector $\hat{\tau}$ for each turgid configuration triangle that describes the direction from the center of the triangle to the tip position of the cell. Additionally, we define any direction in the local tangent plane of the triangle as: $\hat{v}(\phi) = \cos(\phi) * \hat{x}_1^b + \sin(\phi) * \hat{x}_2^b$, where $\{\hat{x}_1^b, \hat{x}_2^b\}$ is a local basis on the turgid triangle, and ϕ is an angle between $\hat{v}$ and $\hat{x}_1^b$. In particular, we use the local principal stretch directions as the local basis. The circumferential direction is then defined as the vector most perpendicular to $\hat{\tau}$: $\hat{v}(\phi^*) \cdot \hat{\tau} = 0$. Then we denote $\hat{v}^\theta = \hat{v}(\phi^*)$. The meridional direction is the vector most aligned with $\hat{\tau}$ and is equal to $\hat{v}^s = \hat{v}(\phi^* \pm \pi/2)$. This process is repeated to establish $\hat{v}^s$ and $\hat{v}^\theta$ on the tangent plane of each triangle (Fig 1E, $\hat{v}^s$ and $\hat{v}^\theta$ arrows).

The circumferential and meridional directions in the turgid configuration can be used to calculate the corresponding stretch ratios, λ_θ and λ_s. Since the optimized directions live on the turgid plane, we use $\mathbf{F}^{-1}$ to transform them to the unturgid plane. Therefore, the ratio of length change before and after the deformation along $\hat{v}^\theta$ and $\hat{v}^s$ is the magnitude of the original turgid vector over the magnitude of the transformed unturgid vector:

$$\lambda_s = \|\hat{v}^s\|/\|F^{-1}\cdot\hat{v}^s\| = 1/\|F^{-1}\cdot\hat{v}^s\|$$
$$\lambda_\theta = \|\hat{v}^\theta\|/\|F^{-1}\cdot\hat{v}^\theta\| = 1/\|F^{-1}\cdot\hat{v}^\theta\| \tag{14}$$

To find $\bar{\kappa}_s(\alpha)$ and $\bar{\kappa}_\theta(\alpha)$ on the wall surface, we use the principal directions on each wall outline point instead of triangle, and the principal curvature directions will be used as the local basis. From there, we define ψ as the angle between a principal direction associated with curvature $\bar{\kappa}_1$ and the local meridional direction, $\hat{v}^s$. Using Euler's equation [41], the meridional curvature is given by:

$$\bar{\kappa}_s = \bar{\kappa}_1\cos^2\psi + \bar{\kappa}_2\sin^2\psi$$
$$\bar{\kappa}_\theta = \bar{\kappa}_2\cos^2\psi + \bar{\kappa}_1\sin^2\psi \tag{15}$$

The final calculation of $\bar{\kappa}_s(\alpha)$ and $\bar{\kappa}_\theta(\alpha)$ on each triangle comes from the average values of each triangle's corresponding points (Fig 2E triangle to Fig 2G).

Computation of mechanical properties in $f(\alpha)$: With the curvatures on each wall outline point, we use Eqs 5 and 6 to calculate the dimensional wall tensions, $\bar{\sigma}_s$ and $\bar{\sigma}_\theta$. The final tensions on the triangle also come from averaging the point-wise tensions. Along with λ_θ and λ_s, we can now use Eq 9 to calculate the dimensional bulk modulus, $\bar{K}_h$ in the regime of $f(\alpha)$. There is an alternative to Eq 9 to calculate the bulk modulus that does not require the deformation gradient. From Eq 9, we can see the term $\lambda_s\lambda_\theta$, which describes the area change of a triangle between the two configurations. This is approximately equivalent to S_B/S_A, where S_B and S_A are the triangle areas in the turgid and unturgid, respectively. The alternative calculation of $\bar{K}_h$ uses the triangulations of the two configurations, and then S_B/S_A instead of $\lambda_s\lambda_\theta$.

The last conversion to the outline model will be to redefine a location marker compatible with the triangulation. We use the local angle α as the positioning coordinate such that different cell sizes can be considered and combined. To calculate α, we first orient the cell towards a central long axis, $\hat{z}$. Depending on the orientation of the cell in the acquired image, a new long axis, $\hat{\tilde{z}}$ (see Fig 1E $\hat{\tilde{z}}$ arrow), needs to be found in an optimal sense. Then we use $\hat{\tilde{z}}$, and each wall outline point's outward normal vector, $\hat{n}$, to calculate a local angle α with the equation $\alpha = \cos^{-1}(\hat{n}\cdot\hat{\tilde{z}})$ (Fig 1E, bottom right triangle). Since each triangle covers multiple wall points, we assign a range of α values to each triangle (S1 Fig). This range is then used to bin any parameter results for each triangle (see Section 1.4 in S1 Text). Through these conversions, the related properties are transformed from $f(u,v)$ to $f(\alpha)$ (Fig 1 workflow).

Synthetic cell framework and estimation of procedure noise

Simulated *P. patens* cell wall surfaces: We adapted upon the previous inference methods using a synthetic cell outline [28, 29], by generating two types of 3-dimensional simulated cells. To explore different morphologies, we have made use of two types of *P. patens* tip-growing cells. The caulonema cell is more tapered, and the chloronema cells are more round [42] (Section 1.1, S1 Text). We have found that their canonical shapes match well with a hyphoid shape which can be described by the equation:

$$x = \frac{\pi y}{a}\cot(\pi y) - \frac{1}{a} \tag{16}$$

where a is the parameter controlling the tapered nature of the cell [43]. Through the fitting of multiple experimental cell outlines, we determined a values for the two cell types (Fig 3A and S3 Fig).

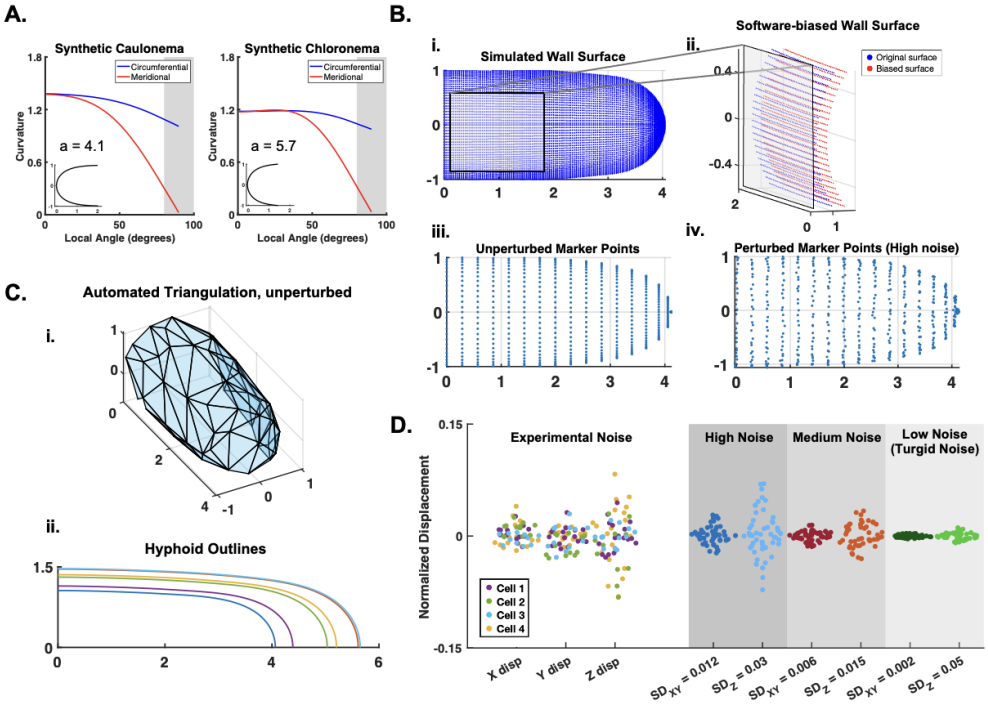

Fig 3. Synthetic cell framework and noise estimation. A. Synthetic caulonema and chloronema cell shape (insets) with circumferential and meridional curvature. The shape is obtained by the hyphoid-function fitting with a single parameter "a" (Eq 16, S3 Fig). Gray region denotes the cell side. **B. (i)** Simulated cell surface **(ii)** Software-biased wall surface (red) compared against the original wall surface points (blue). Bias can occur outwardly or inwardly. **(iii).** Unperturbed cell marker points **(iv).** Perturbed cell marker points (high noise). **C. (i.)** Example synthetic cell triangulation with unperturbed marker points. **(ii).** Collection of synthetic caulonema cell outlines with different widths, to mimic size variation in reality. **D.** (Left) Noise estimation from experiments (see Methods). Data taken from n = 4 cells separated into X, Y, and Z displacement. Displacement was normalized by the cell radius. (Right) Replicated synthetic noise for three cases: high, medium, and low. Values are drawn from a normal distribution with mean = 1 and SD shown for each corresponding column.

We input $\bar{K}_h$ and $\bar{\mu}_h$ on the unturgid hyphoid outline using the distributions previously established (see Cell wall mechanics model). Our computational model will solve for the corresponding turgid outline. To recreate the wall outline, we discretized the hyphoid outlines into 129 points. We additionally, discretized the hyphoid outlines into 17 points to create the set of initial marker points to select from. Both sets of points are then rotated about the long axis, thereby constructing the configurations of the three-dimensional cell wall surfaces (Fig 3B, i,iii). For each inference, we apply our automated triangulation scheme (Fig 1D) onto a subset of marker points (Fig 3C, i). Cells are given a random size within a range that covers variation observed in reality (Fig 3C, ii).

Local elastic stretch ratio using change in radii: To apply the procedure described in [27] to measure the wall surface modulus, Y, we used our turgid and unturgid hyphoid cell outlines. To match the parameters of their wall model, we set Poisson's ratio (ν) equal to 0. Then, in relation with the bulk modulus, $2K_h = Y$. We

generated caulonema and chloronema cells with this condition and three cases of elastic moduli distributions: constant, nonlinear, and linear. For the cell side, we used the formula: $Y_{side} = \frac{R_B}{(R_B - R_A)/R_A}$ where R_B and R_A are the radii of the cell side in the turgid and unturgid configurations, respectively. At the tip, we used the formula: $Y_{tip} = \frac{R_B}{2(R_B - R_A)/R_A}$. In both instances, we have used a rescaling of the formulas to remove the pressure ($\bar{P}$), and cell wall thickness (h). Given that it was not reported how tip radius was measured, we used a range of degrees of coverage of the wall outline. For each range, we used a sphere-fitting function to find the best fit sphere for the turgid and unturgid cells [44] (S5 Fig).

Origins of noise on the marker points and cell wall outline: We used the Ridge Detection software in ImageJ [45,46] to extract the tagged cell wall outline (Fig 1A, 2C). The software is quite robust in centering the wall outline in the fluorescent signal, as well as maintaining the smoothness of the curve. Therefore, we attributed the noise to the software's ability to detect the real cell wall given the quality of fluorescence signal. To recreate this, we have added noise to the outline data by moving the wall surface outlines outwardly or inwardly along the normal direction (Fig 3B, ii).

We used the software RS-FISH, a fluorescent spot detector applied in ImageJ, to locate our marker points [47]. From their work, we have estimated that their accuracy is within 1% of the cell width of our synthetic cells, with larger error in the z-direction. This noise would be applied to both the turgid and unturgid marker points. The larger aspect of marker point noise comes from the imaging setup itself, including the disturbances in the experimental setup and microscope capabilities. We have estimated the experimental setup noise by imaging the random movement of fluorescent beads on a cell (see Section 1.2 in S1 Text). We found that the results followed a normal distribution, with the noise in the z-direction being twice that of the x-y-directions (Fig 3D, left). We set three noise levels on the unturgid cell using normal distributions with different standard deviations (Fig 3D, right). These can be added to the synthetic unturgid marker points to replicate noise on the marker points during the experiment (Fig 3B, iv). The largest noise case follows the standard deviation of the measured experimental noise. The smallest noise case is when there would only be noise from the software itself, so the unturgid and turgid marker point noises are equal. We estimated the software noise to have a standard deviation of 0.002 in the x-y-plane and standard deviation of 0.005 in the z-plane (Fig 3D, right). The noise values, denoted δ, have all been rescaled by the cell radius: $\delta \to \bar{\delta}/\bar{L}$.

Results

Inference of elasticity gradient in single cells with no noise

The parameter sensitivity study of our surface morphology-based method (Figs 1, 2, S1 Fig, S2 Fig) will begin by testing the spatial surface bulk modulus (K_h) inference with no noise. To represent different possible K_h distributions, we consistently inferred three cases of cell elastic moduli distributions: constant, nonlinearly, and linearly decreasing (see Methods). We will apply the methodology on simulated tip surfaces matching cells from moss protonema in *Physcomitrium patens*. The two cell types will include the more tapered caulonema cell and the rounded chloronema cells (Fig 3A-C, S3 Fig). To organize the results, we will primarily present on the caulonema shape, with comparisons to the chloronema shape when different cell shapes affect the inference outcome.

Sphere-fitting method is sensitive to cell shape: We first wanted to infer the wall

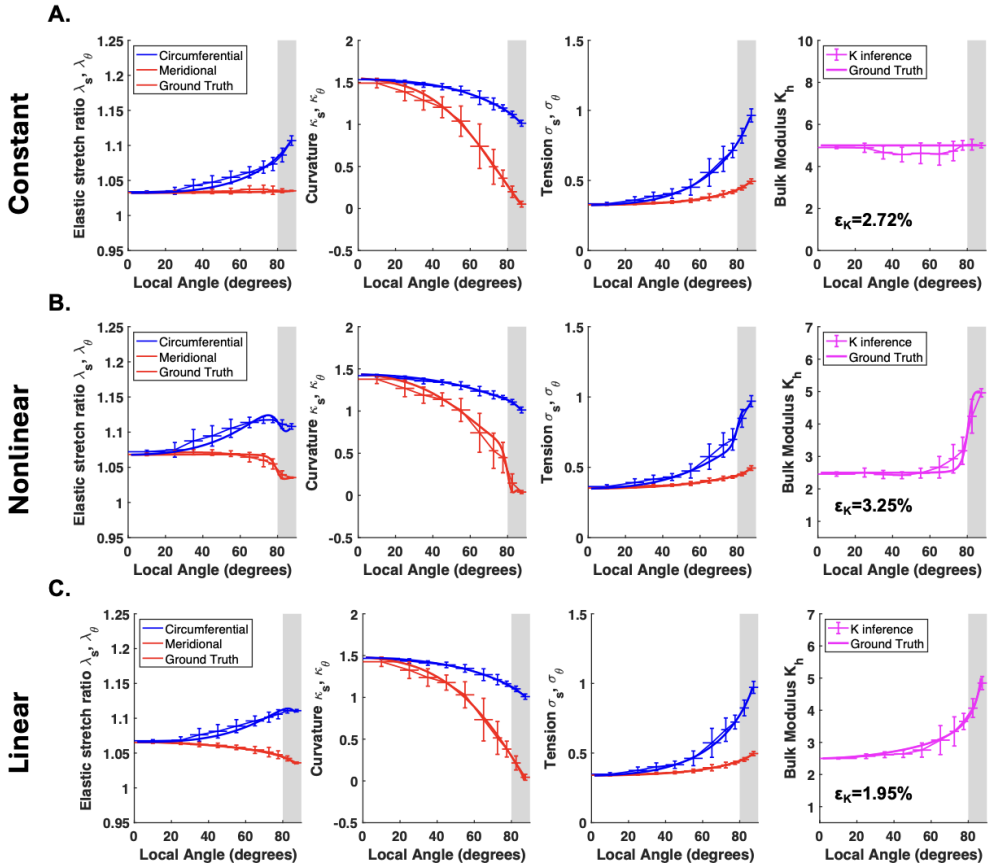

Fig 4. No noise inference of geometric parameters in synthetic caulonema cells. Inference results of **A.** constant, **B.** nonlinear, and **C.** linear distributions using the triangulation scheme on one synthetic caulonema cell. In each case, the elastic stretch ratio, curvature, and tension inferences are shown with their corresponding ground truth values. The rightmost panels depict the bulk modulus inference along with their relative error from the ground truth, ε_K. Note that the curve will be linear when plotted as a function of z, instead of α. Values are non-dimensionalized ($\kappa_{s,\theta} = \bar{\kappa}_{s,\theta}\bar{L}$, $\sigma_{s,\theta} = \bar{\sigma}_{s,\theta}/\bar{P}\bar{L}$, $K_h = \bar{K}_h/\bar{P}\bar{L}$).

surface modulus (Y) published in [27], which is in the same dimension of K_h. The formulas read: $Y_{side} = \frac{R_B}{(R_B-R_A)/R_A}$ and $Y_{tip} = \frac{R_B}{2(R_B-R_A)/R_A}$, where R_B and R_A are the radii of the cell in the turgid and unturgid configurations, respectively (see Methods). We tested this method by using the wall surface of synthetic caulonema and chloronema cells with varying elastic moduli distributions (constant, nonlinear, and linear S5 Fig). At the side, our estimate in both cell types were always within 5% error of the ground truth Y_{side} (not shown). However, at the tip of the cell, we found that R_A and R_B varied depending on the range of cell wall surface points used to fit the sphere (S5 FigA, C). The more tapered caulonema cells with constant and linear elastic moduli had good inference of the modulus when a smaller selection was used, specifically for 10-20 degrees (S5 FigB). The nonlinear graded cell inferences were all underestimated. Strikingly, the chloronema cells gave non-physical results due to R_A being larger than R_B, leading to negative values of Y_{tip} (S5 FigC, D). Although each chloronema case had a good inference using a selection of 60 degrees, the overall results were inconsistent. From this result, we reasoned that the complexity of elastic deformation at the tip in

rounder cells could not be directly captured by the change in tip radius. Although we acknowledge that this method could work for more tapered cells, we move forward with investigating the inference with our marker point method (Figs 1, 2) to measure K_h.

Marker point tracking can accurately infer elasticity with no noise: Using the marker point triangulation scheme (Figs 1, 2), the elastic stretch ratio, curvature, and tension parameters were all well inferred from the wall surface (Fig 4). Consequently, the averaged error of K_h, denoted ε_K, was within 4% error in all three cases and in both caulonema and chloronema cells (see Fig 4 and S6 FigA-C, respectively). We also inferred K_h using the triangle area change instead of $\lambda_s\lambda_\theta$, and the two results were virtually identical (S6 FigD). From here, we investigated how the size of the triangulation would affect the precision of our method with no noise. We present three triangulation cases with different averaged sizes, $\bar{\Delta}_A/\bar{L}^2$, where $\bar{\Delta}_A$ is the mean triangle area, and $\bar{L}$ is the cell radius. These are obtained by changing the initial number of marker points chosen, N_Δ, and normalized filtering distance d_Δ (see Methods). The three cases are visually distinguishable, with different distributions of normalized triangle areas (S7 FigA). We found that the error in K_h in the large triangulated cell came from the increased deviations from the ground truths at the tip as the triangulation size increases (S7 FigB-D). This can be explained by the larger triangles covering a large local angle range (see S1 Fig). When there is a steeper change of a property (like λ_θ or σ_θ) within a small angle range, large triangles will span multiple angle bins and affect the overall average in each bin, especially at the tip. To put this back into the perspective of the cell wall surface, we mapped the trend of $\lambda_s\lambda_\theta$ on each triangulation (Fig 5A). We can observe the smaller $\bar{\Delta}_A/\bar{L}^2$ case gives the best resolution of the gradient of $\lambda_s\lambda_\theta$.

Inference of elasticity gradient in single cells with noise

To quantify levels of noise, primarily from the marker point localization, we used our experimental setup to obtain an estimate (Fig 3D, Methods). Our reported standard deviation values representing the noise δ are normalized to our cell radius $\bar{L}$, namely $\delta/\bar{L}$ (Fig 3D). After adding them to our synthetic cell triangulations, we first observed the effect of noise on the single cell triangulation level (Fig 5B-5D). At the lowest noise level (Fig 3D), we can see the loss of the smooth gradient of $\lambda_s\lambda_\theta$ and an overall increase in the averaged error, ε_K, compared to no noise. Notably, the correlation between error and triangulation size was disrupted at the low noise level, as the smallest triangulation exhibited the greatest error (Fig 5B). We can observe that the small triangulated cell surface becomes more heterogeneous in comparison to the other two sizes. This patterning becomes more pronounced in all cases at the next two levels of noise (Fig 5C-D). There is no clear trend of ε_K among different noise levels due to the randomness of noise. However, the large triangulation is the most stable across all noise levels. As the triangulation gets smaller and the noise gets higher, there is increased susceptibility to noise because the ratio of marker point displacement from noise to triangle size is smaller. Considering that the results of a single cell can suffer from the randomness, we explore multiple cells to infer the mean-property against the ground truth.

Effect of multiple cell data on inference accuracy: Assuming a mean-distribution of elastic moduli exists among a group of cells, we analyzed how the inference from multiple cells helps to approach the underlying property. To implement this, we leveraged our synthetic cell data to create multiple hyphoid cells with the same ground truth elastic moduli distributions (see Fig 3C, ii). Each cell was given a random width within a range to replicate different experimental cell sizes. Then we applied our inference procedure to each cell with different triangulations and random noise, and

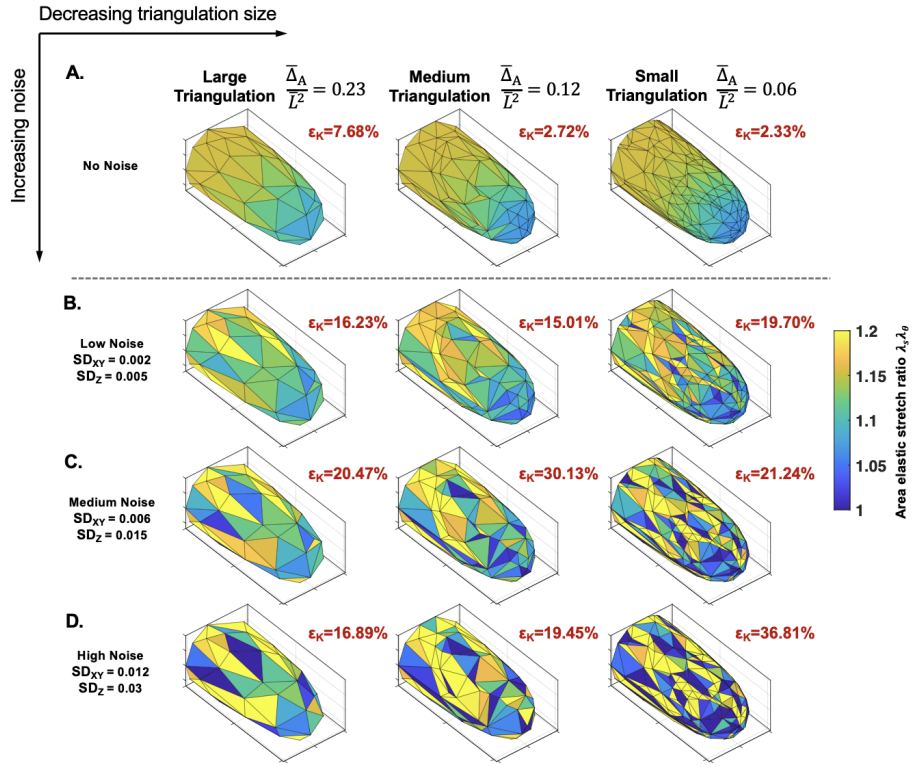

Fig 5. Effects of triangulation size and noise on a single cell: For each triangulation size, the same triangulated cell is shown with increasing noise on the marker points: **A.** no noise, **B.** low noise, **C.** medium noise, and **D.** high noise. Each triangle is colored by their area elastic stretch ratios: $\lambda_\theta \lambda_s$. Triangles with values outside the bounds of the color bar are assigned the colors at the boundary. The ε_K value shows the corresponding K_h error for each cell, and are calculated after filtering triangles with $\lambda_s \lambda_\theta < 1$. All cells shown have a ground truth of $K_h = 5$, constant.

averaged the K_h results at increasing cell sample sizes (see Section 1.4 in S1 Text).

We first analyzed the trend when the lowest amount of noise was added (S8 Fig). As anticipated, we saw that the mean relative error had a sloping behavior with an initial drop as the trial number went up. As an optimization problem of error versus trial number, we reported the "knee" of the curve and corresponding averaged error at that point ($\bar{\varepsilon}_K$) [48]. In the lowest noise level, we observed the disrupted triangulation trend seen in Fig 5, but with overall improved inference (S8 Fig). Although, the medium triangulation performed the best overall at the low level of noise, once we increased the noise to the medium level, the large triangulation started performing the best (S9 Fig). The overall error was significantly increased at the highest level of noise, but the largest triangulation remained with the best result (S10 Fig). We further found that we could effectively increase our data without adding additional samples by adding another triangulation on the same cell (S1 Text, Section 1.4). Although the decrease in the overall error was not significant, we noticed that this helped decrease the knee value (S10 Fig, S11 Fig). We applied this two triangulation method to our subsequent analyses. Ultimately, we concluded that $n = 10$ cells, each with two triangulations, was an optimal sample number given the level of noise from experiments, for minimizing both the error and sample size.

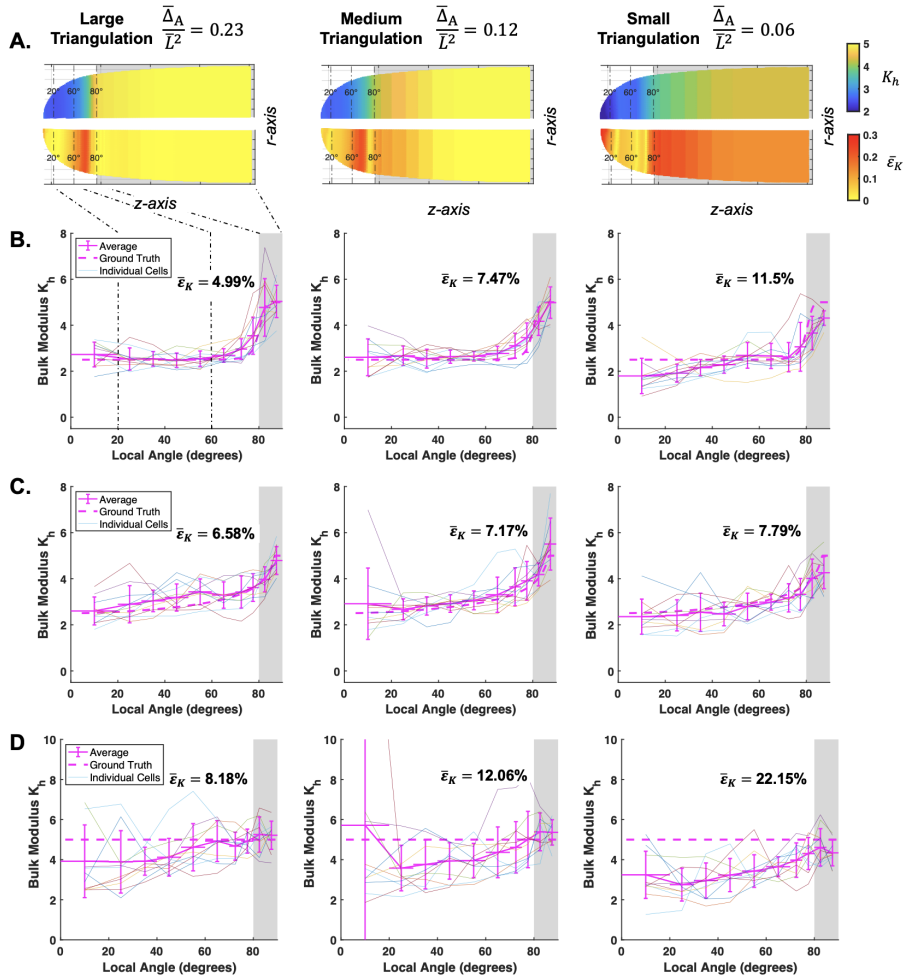

Fig 6. Inference of bulk modulus with high noise can be recovered with multiple cell averaging A. Averaged result of n = 10 cells interpolated back onto a synthetic caulonema cell (top). Averaged error ($\bar{\varepsilon}_K$) shown on the synthetic cell (bottom). Dashed lines denote local angle reference markers on the cell. The spatial results along the local angle are shown for a **B.** nonlinear, **C.** linear, and **D.** constant case. Each individual cell result and ground truth bulk modulus are plotted behind. Modulus values are non-dimensionalized ($K_h = \bar{K}_h/\bar{P}\bar{L}$).

Sensitivity of gradient recovery against large perturbations: The importance of this method is its ability to capture a spatial distribution of elastic modulus. Through averaging the standard $n = 10$ cells, the nonlinear gradient was recovered in all three triangulation cases and re-established on the synthetic cell wall surface (Fig 6A, K_h). The corresponding averaged error distribution is shown as well (Fig 6A, $\bar{\varepsilon}_K$), demonstrating that the large and medium triangulations typically suffer at the sharp transition region. Interestingly, the small triangulation has higher error at the side and tip, but has better accuracy at the transition area, improving its error overall (see also S11 FigB, C insets). The linear results performed similarly well to the nonlinear, with overall better inference since the methodology does not suffer due to a sharp transition (Fig 6B, C).

We found there rarely were instances of false negative gradients since K_h was not frequently overestimated at the tip. However, the occurrence of a false-positive gradient

result in cells with constant elastic moduli became a problem. We first noticed this trend occurring in the small triangulated cells with medium noise (S9 FigA insets). With high noise (Fig 3D), there was a significant increase in the number of decreasing gradients in cells with constant elastic moduli in all three triangulation cases (S11 FigA). Given the frequency of these false gradients, the ground truth constant distribution was not fully recovered after obtaining the average inference of 10 cells (Fig 6D).

We reasoned that the overall underestimation at the tip is due to values of $\lambda_s\lambda_\theta$ approaching 1. When this occurs, K_h is susceptible to perturbations because its denominator approaches 0 (Eq 9). The constant case of $K_h = 5$ has lower values of $\lambda_s\lambda_\theta$ at the tip, compared to the tip of the graded cases (see Fig 4 first column). When noise is added, the elastic stretch ratio measurements balance around the ground truth, but at a ground truth of $\lambda_s\lambda_\theta \approx 1.06$, many of the values will fall below 1, causing negative K_h values. After filtering the triangles whose $\lambda_s\lambda_\theta < 1$, we are left with triangles that fall above the ground truth. This unbalance of higher elastic stretch will correlate with an underestimation of K_h. Generally, the coupling effect between K_h and the cell geometry means that more tapered cells will generally suffer more since they are under less tension and thus have lower values of elastic stretch. We confirmed this in the rounder chloronema cells, showing that although the false-positive problem remains in the constant case, the false gradient is flatter (S12 FigA). In general, there is also poorer inference at the tip due to there being inherently less triangles available there compared to the cell side. Seeing that a cell with constant $K_h = 5$ could lead to incorrect spatial inferences, it was logical to investigate how K_h affects a false-positive outcome. Moreover, investigating more case scenarios would allow us to determine a more global result of inference accuracy, especially given a broader set of cell types and experimental set-ups.

Global sensitivity to noise and triangulation size

Given the uncertainty of the tip-growing cell wall elasticity, especially with varying turgor pressure and cell size, we expanded our search to include a range of possible distributions of elastic moduli. We covered a range of unique cases of surface K_h side and tip values, including constant and gradient cases, which were given a nonlinear distribution (S1 Movie, S2 Movie). For each case, we inferred the standard 10 cells repeatedly, and used their averaged inference to calculate the inferred endpoint ratio: $\frac{K_{side}}{K_{tip}}$ (S1 Text, Section 1.4). The final results were interpolated across the grid (Fig 7). At the lowest level of noise, the three triangulation resolution results are similar (Fig 7A). The top right corner of each map has the lowest values of elastic stretch, and we can see the contour distortions start there in the small triangulation map as noise is increased (Fig 7B). This begins to affect the large and medium triangulations when the noise is further increased (Fig 7C). We further confirmed that the chloronema results with the same range of K_h performed better overall (S13 Fig). This is again due to the coupling between tension and K_h, causing higher elastic stretch ratios and thus, more accurate results (S2 Movie).

To interpret the mapping in more detail, we can see how the problem of false-positivity corresponds with the contour expansions. For example, any measurement of $\frac{K_{side}}{K_{tip}}$ in the range of 1.2-1.4 with a K_{side} higher than 5, could mean a false-positive measurement of a gradient (Fig 7C, large triangulation). The reason being the invasion of the adjacent group ($K_{side}/K_{tip} = 1.4$) into the lowest level. With that same logic, the confidence range is reduced in the medium triangulation, and further reduced in the small triangulation with a range of $K_{side}/K_{tip} = 2$ included (Fig 7C). However, in the rounder chloronema cells, the large triangulation can confidently measure a constant K_h up until the uppermost corner (S13 FigC, left column). To

quantify a direct value of reliability, we overlaid the values of the averaged error ($\bar{\varepsilon}_K$) of the inference and the endpoint ratio error, $\bar{\varepsilon}_{K_{side}/K_{tip}}$ (see below).

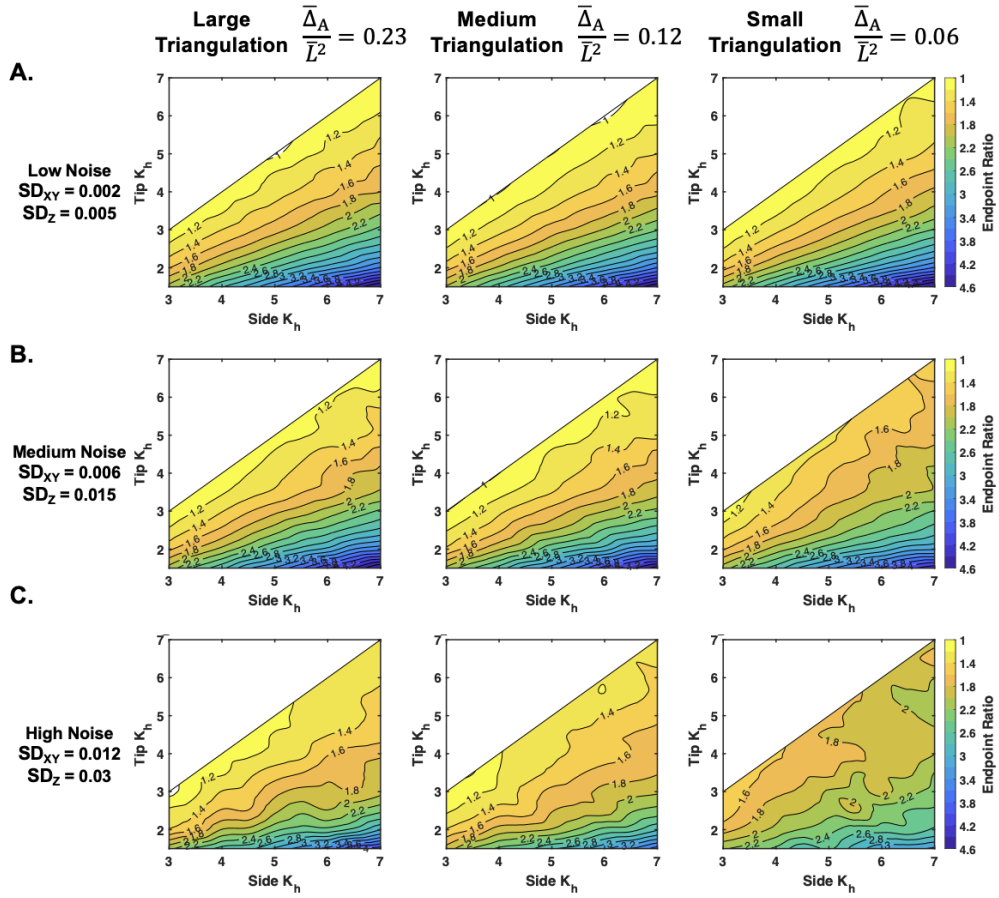

Fig 7. Inferred endpoint ratio results across different triangulation sizes and noise levels from a synthetic caulonema cell. Contour map depicts the inferred endpoint ratio levels (K_{side}/K_{tip}) across a range of K_{side} and K_{tip} values at the three triangulation sizes and different noise levels: **A.** low noise, **B.** medium noise, and **C.** high noise. Results come from repeating the averaging of the standardized 10 cells to remove random effects (see S1 Text). Modulus values are non-dimensionalized ($K_h = \bar{K}_h/\bar{P}\bar{L}$).

Two error quantification mappings reveal locations of reliable inference: The center of the averaged error map for caulonema and chloronema cells is consistently within 10% error, reinforcing our results from Fig 6 (Fig 8A, B). But as suspected, the upper right corner of the phase map where the moduli are high and the elastic stretch ratios are low, has higher error values in the small triangulation map. On the other hand, the endpoint ratio error more clearly reflects the underestimation of K_{side} and/or K_{tip} (Fig 8C, D). The absolute value is shown, but there is a transition from positive ratio error to negative along the middle of the map. As the ratio increases towards the bottom right of each map, we found that the method may not accurately infer the nonlinear distribution's sharp transition due to the bin size. This typically caused underestimation of K_{side}, leading to negative $\bar{\varepsilon}_{K_{side}/K_{tip}}$. Error in the top right came from underestimation of K_{tip} (Fig 8C, D). The edge of the lowest level set

($K_{side}/K_{tip} = 1.2$) can be seen corresponding to about a 20% endpoint ratio error (Fig 8C, black 1.2 line and white dashed lines). We translated this to be a reasonable value of error bordering the false-positivity problem, and highlighted this boundary in both error maps (Fig 8, white dashed lines). We also used 5% error as a stricter experimentally acceptable error boundary, which showed the triangulation size trend through the increase of the bounded area from small to large triangulation (Fig 8C, D white dotted lines). As expected, at lower levels of noise, the thresholds of 5% and 20% error are expanded (S14 Fig and S15 Fig). The chloronema endpoint ratio error results for the large triangulation were all within 20% error (Fig 8D, left). Finally, our results inferring K_h with the triangle area change instead of $\lambda_s\lambda_\theta$ continued to be virtually identical (not shown).

Discussion

The spatial cell wall elasticity in tip-growing cells is one determining factor of where plant cell walls grow, making them an important measurement for tip growth models. Here, we presented a systematic analysis of a new method to measure the elastic properties of the cell wall. By using a surface triangulation method to connect marker points across the cell surface, we were able to adopt the axisymmetric mechanical model to measure the wall elastic moduli (Fig 1, 2). Through our parameter study, we found that a coarser triangulation size was more robust against noise and that a sample size of 10 cells was necessary to recover the ground truth in all cases with noise. Using that number, we created a reference map encompassing a range of elastic moduli distributions, which could be used to verify inference reliability. Throughout our study, we presented dimensionless variables with the aim that this method can be adapted to any walled system. This could open many avenues for experimentalists to incorporate measured cell wall properties into tip cell mechanical modeling.

The primary significance of our method is that it aims to measure the wall properties within a small region between the cell side and tip, which we call the transition region. This measurement is particularly relevant given that modeling work has posited that sharp gradients of wall mechanics occur in that region [18–20]. However, adapting techniques to confirm this in an experimental framework has been challenging. A more straightforward approach targeting the general tip and side areas was used to find a gradient in filamentous fungi [27], but when we applied their method synthetically we found that it inconsistently inferred the wall modulus at the tip (S5 Fig). Given the uncertainty of experimental approaches, it was important to us to perform a parameter sensitivity study to support future experimental measurements. Typically, we have seen techniques like finite element modeling being used to verify indentation results [49, 50], but we have not seen this done extensively for other tip-growing cell measurement methods. We used a simpler approach by adapting synthetic marker points onto simulated cell surfaces with a ground truth elastic moduli (Fig 3). Since we did not know how cell morphology may affect the inference of these cell wall properties, we utilized the *P. patens* cells at our disposal. The canonical caulonema and chloronema cell types provided a point of comparison between a tapered and round morphology, respectively (Fig 3). Using our marker point methodology, we were able to verify good inference accuracy in both synthetic cell types with no noise (Fig 4). Importantly, we found that the method was able to accurately measure the cell wall elasticity changes in the transition region.

By studying the dimensionless parameters, the presented results can be interpreted to any walled system with different osmotic pressures, cell sizes, and experimental marker point techniques. We have introduced these non-dimensionalized parameters throughout this article, such as the noise on the marker points $\delta/\bar{L}$, triangulation

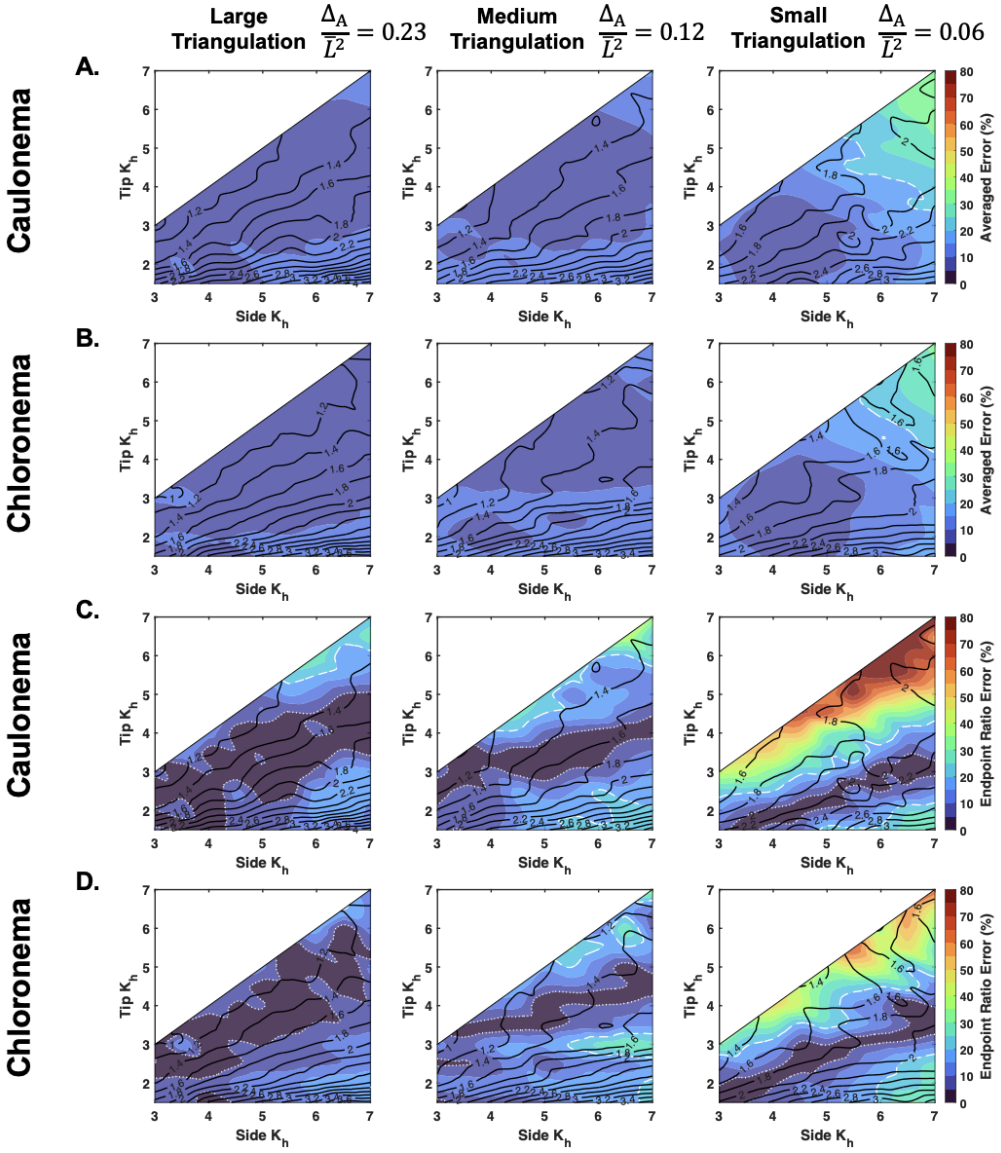

Fig 8. Two error quantifications for caulonema and chloronema cell bulk modulus inference with high noise Averaged error ($\bar{\varepsilon}_K$) for **A.** caulonema and **B.** chloronema cells. Relative absolute value endpoint ratio error ($\bar{\varepsilon}_{K_{side}/K_{tip}}$) for **C.** caulonema and **D.** chloronema cells. In all parts, the underlying contours from Fig 7 (caulonema) and S13 Fig (chloronema) are shown. The white dashed line denotes the boundary of 20% error and the white dotted line denotes the boundary of 5% error. Results come from repeating the averaging of the standardized 10 cells to remove random effects (see S1 Text). Modulus values are non-dimensionalized ($K_h = \bar{K}_h/\bar{P}\bar{L}$).

resolution $\bar{\Delta}_A/\bar{L}^2$, and the dimensionless elastic moduli $K_h = \bar{K}_h/\bar{P}\bar{L}$. The noise affecting the marker point positions was estimated from our experimental setup (Fig 3D), and will depend on the cell width. The size of the cell as well as potential experiment setup differences is why we presented different levels of noise throughout (Figs 5, 7, 8). The type and adhesion of experimental marker points will be an experimental constraint in each walled cell system. Our preliminary testing used fluorescent microspheres with application through liquid flow onto the tip cell (Fig 1A),

although we have seen other dependable techniques [20, 23]. Given the uncertainties of the marker point distributions, we took advantage of our synthetic marker points to study how different triangulation sizes affected the inference results. Our previous findings showed that a courser spacing of marker points was more stable against noise [29], and we similarly concluded here that using a larger triangulation gave the most stable results (Figs 5-8). Thus, regardless of the number of marker points, our recommendation would be to use a larger triangulation, relative to the cell size. One's final triangulation sizes can be benchmarked by the dimensionless parameter representing the triangle areas, $\bar{\Delta}_A/\bar{L}^2$ (Figs 5-8).

From what has been published, most walled cells have sufficient elastic stretch for this method to be feasible [9, 23, 27, 29]. This is a key criteria in the inference of K_h, due to the presence of the elastic stretch ratios in the denominator. When $\lambda_s\lambda_\theta < 1$, non-physical values of K_h appear. Since these non-physical values do not appear when there is no noise in the system, it is clear that our measurements are impaired by $\delta/\bar{L}$ and the resultant filtering of values. At the tip of the cell where there is less data, the triangulation and therefore $\lambda_s\lambda_\theta$ are even more susceptible to perturbations. In cells with a constant distribution, the underestimation of K_h at the tip uncovered a false-positive gradient problem. We mapped the presence of this problem on contour maps, confirming that most bulk modulus distributions could be recovered using multiple cell samples and a larger $\bar{\Delta}_A/\bar{L}^2$ (Figs 7, 8). The reference maps highlight which areas can and can not be recovered so that one can use them to confirm the reliability of a measurement. Although we acknowledge the reference maps may not be applicable to morphologies at the more extreme ends of the shape spectrum [4, 35], the generalized interpretation can be made with a tapered and round tip morphology.

Our future work will be to continue to apply this method to measure the bulk modulus distribution in the two types of *P. patens* tip cells. Once we have obtained a reliable measurement guided by Figs 7 and 8, we will be able to scale it using estimates of turgor pressure $\bar{P}$, wall thickness h, and cell radius $\bar{L}$. As a demonstration of this scaling, we first approximated the turgor pressure in *P. patens* to be $\bar{P} \approx 0.75$ MPa, comparable with findings in fungal tips and brown algae [9, 27]. Those same publications also provide estimates for the cell wall thickness similar to measurements made in *P. patens* at $h \approx 260$ nm [51]. We can first estimate the wall stresses, which are the wall tensions divided by the wall thickness, $\bar{\tilde{\sigma}}_{s,\theta} = \frac{\bar{P}\cdot\bar{L}}{h}\sigma_{s,\theta}$. Using also $\bar{L} \approx 10\ \mu m$, our estimate of wall stress would fall in the range of $\bar{\tilde{\sigma}}_{s,\theta} \approx 30$ MPa, consistent with previous reports [4, 9, 20, 34]. Likewise, the bulk modulus can be calculated with the equation $\bar{K} = \frac{\bar{P}\bar{L}}{h}K_h$. The dimensionless range of $3 \leq K_h \leq 7$ used in Figs 7 and 8, was motivated by our estimates of elastic stretch. Consequently, we expect cells with similar ranges of $\bar{P}, \bar{L}$ and h to have bulk modulus values in the range of 90 to 200 MPa, comparable to estimates in yeast and fungal cell walls [23, 27]. Having this measurement in multiple systems will provide perspective on how different cell types modulate their wall elastic moduli to adapt to different growth rates and morphologies. We will also plan to explore the method limitations shown here, specifically the measurement of the shear modulus. Having the measurement of both elastic moduli will be essential to fully describe the wall material and model how the mechanics modulate tip cell growth and morphogenesis.

Acknowledgments

M.W. and R.X. acknowledge partial funding from the National Science Foundation - Division of Mathematical Sciences (NSF-DMS) grant DMS-2012330 and DMS-2144372 (CAREER). L.V. acknowledges partial funding from the National Science Foundation - Division of Molecular and Cellular Biology (NSF-MCB) grant MCB-2154573.

References

1. Benkert R, Obermeyer G, Bentrup FW. The turgor pressure of growing lily pollen tubes. Protoplasma. 1997;198:1–8.
2. Cosgrove DJ. Growth of the plant cell wall. Nature reviews molecular cell biology. 2005;6(11):850–861.
3. Fischer-Friedrich E, Hyman AA, Jülicher F, Müller DJ, Helenius J. Quantification of surface tension and internal pressure generated by single mitotic cells. Scientific reports. 2014;4(1):6213.
4. Ohairwe ME, Živanović BD, Rojas ER. A fitness landscape instability governs the morphological diversity of tip-growing cells. Cell Reports. 2024;43(4).
5. Galway M. Root hair cell walls: filling in the framework. Botany. 2006;84(4):613–621.
6. Hepler PK, Rounds CM, Winship LJ. Control of cell wall extensibility during pollen tube growth. Molecular Plant. 2013;6(4):998–1017.
7. Bibeau JP, Galotto G, Wu M, Tüzel E, Vidali L. Quantitative cell biology of tip growth in moss. Plant molecular biology. 2021; p. 1–18.
8. Bartnicki-Garcia S, Bracker CE, Gierz G, López-Franco R, Lu H. Mapping the growth of fungal hyphae: orthogonal cell wall expansion during tip growth and the role of turgor. Biophysical journal. 2000;79(5):2382–2390.
9. Rabillé H, Billoud B, Rolland E, Charrier B. Dynamic and microscale mapping of cell growth. Protocols for Macroalgae Research; CRC Press: Boca Raton, FL, USA; Taylor & Francis: Oxfordshire, UK. 2018; p. 349–364.
10. Durachko DM, Park YB, Zhang T, Cosgrove DJ. Biomechanical characterization of onion epidermal cell walls. Bio-protocol. 2017;7(24):e2662–e2662.
11. Wang X, Wilson L, Cosgrove DJ. Pectin methylesterase selectively softens the onion epidermal wall yet reduces acid-induced creep. Journal of experimental botany. 2020;71(9):2629–2640.
12. Cleland R. Extensibility of isolated cell walls: measurement and changes during cell elongation. Planta. 1967;74:197–209.
13. Geitmann A, Parre E. The local cytomechanical properties of growing pollen tubes correspond to the axial distribution of structural cellular elements. Sexual Plant Reproduction. 2004;17:9–16.
14. Zerzour R, Kroeger J, Geitmann A. Polar growth in pollen tubes is associated with spatially confined dynamic changes in cell mechanical properties. Developmental biology. 2009;334(2):437–446.
15. Chebli Y, Kaneda M, Zerzour R, Geitmann A. The cell wall of the Arabidopsis pollen tube—spatial distribution, recycling, and network formation of polysaccharides. Plant Physiology. 2012;160(4):1940–1955.
16. Lockhart JA. An analysis of irreversible plant cell elongation. Journal of theoretical biology. 1965;8(2):264–275.
17. Goriely A, Tabor M. Self-similar tip growth in filamentary organisms. Physical review letters. 2003;90(10):108101.

18. Dumais J, Shaw SL, Steele CR, Long SR, Ray PM. An anisotropic-viscoplastic model of plant cell morphogenesis by tip growth. The International journal of developmental biology. 2006;.

19. Fayant P, Girlanda O, Chebli Y, Aubin CE, Villemure I, Geitmann A. Finite element model of polar growth in pollen tubes. The Plant Cell. 2010;22(8):2579–2593.

20. Rojas ER, Hotton S, Dumais J. Chemically mediated mechanical expansion of the pollen tube cell wall. Biophysical journal. 2011;101(8):1844–1853.

21. Campàs O, Rojas E, Dumais J, Mahadevan L. Strategies for cell shape control in tip-growing cells. American Journal of Botany. 2012;99(9):1577–1582.

22. de Jong T, Hulshof J, Prokert G. Modelling fungal hypha tip growth via viscous sheet approximation. Journal of theoretical biology. 2020;492:110189.

23. Abenza JF, Couturier E, Dodgson J, Dickmann J, Chessel A, Dumais J, et al. Wall mechanics and exocytosis define the shape of growth domains in fission yeast. Nature communications. 2015;6(1):8400.

24. Spinelli K, Wei C, Vidali L, Wu M. Inferring Exocytosis Profiles from Cell Shapes Using a Dual-Configuration Model of Walled Cell Tip Growth. Journal of Theoretical Biology. 2025; p. 112196.

25. Atilgan E, Magidson V, Khodjakov A, Chang F. Morphogenesis of the fission yeast cell through cell wall expansion. Current Biology. 2015;25(16):2150–2157.

26. Davì V, Chevalier L, Guo H, Tanimoto H, Barrett K, Couturier E, et al. Systematic mapping of cell wall mechanics in the regulation of cell morphogenesis. Proceedings of the National Academy of Sciences. 2019;116(28):13833–13838.

27. Chevalier L, Pinar M, Le Borgne R, Durieu C, Peñalva MA, Boudaoud A, et al. Cell wall dynamics stabilize tip growth in a filamentous fungus. PLoS Biology. 2023;21(1):e3001981.

28. Chelladurai D, Galotto G, Petitto J, Vidali L, Wu M. Inferring lateral tension distribution in wall structures of single cells. The European Physical Journal Plus. 2020;135(8):662.

29. Deng Y, Wei C, Xu R, Vidali L, Wu M. Inferring relative surface elastic moduli in thin-wall models of single cells. The European Physical Journal Plus. 2022;137(8):880.

30. Davì V, Tanimoto H, Ershov D, Haupt A, De Belly H, Le Borgne R, et al. Mechanosensation dynamically coordinates polar growth and cell wall assembly to promote cell survival. Developmental cell. 2018;45(2):170–182.

31. Inc TM. delaunay function; R2023a. Available from: `https://www.mathworks.com/help/matlab/ref/delaunay.html`.

32. Rodriguez EK, Hoger A, McCulloch AD. Stress-dependent finite growth in soft elastic tissues. Journal of biomechanics. 1994;27(4):455–467.

33. Voyiadjis GZ, Yaghoobi M. Nonlocal Continuum Plasiticty. In: Size effects in plasticity: from macro to nano. Academic Press; 2019.

34. Dumais J, Long SR, Shaw SL. The mechanics of surface expansion anisotropy in Medicago truncatula root hairs. Plant physiology. 2004;136(2):3266–3275.

35. Campas O, Mahadevan L. Shape and dynamics of tip-growing cells. Current Biology. 2009;19(24):2102–2107.

36. Inc TM. meshgrid function; R2023a. Available from: https://www.mathworks.com/help/matlab/ref/meshgrid.html?s_tid=doc_ta.

37. Inc TM. griddata function; R2023a. Available from: https://www.mathworks.com/help/matlab/ref/griddata.html?s_tid=doc_ta.

38. Thorpe J. The Weingarten Map. In: Elementary Topics in Differential Geometry. Springer; 1979. p. 53–61.

39. Inc TM. gradient function; R2023a. Available from: https://www.mathworks.com/help/matlab/ref/gradient.html?s_tid=doc_ta.

40. Roberts AW, Roberts EM, Haigler CH. Moss cell walls: structure and biosynthesis. Frontiers in Plant Science. 2012;3:166.

41. Eisenhart LP. A treatise on the differential geometry of curves and surfaces. Ginn; 1909.

42. Menand B, Calder G, Dolan L. Both chloronemal and caulonemal cells expand by tip growth in the moss Physcomitrella patens. Journal of experimental botany. 2007;58(7):1843–1849.

43. Bartnicki-Garcia S, Hergert F, Gierz G. Computer simulation of fungal morphogenesis and the mathematical basis for hyphal (tip) growth. Protoplasma. 1989;153(1):46–57.

44. J M. Object-oriented tools to fit/plot conics and quadrics; 2025. https://www.mathworks.com/matlabcentral/fileexchange/87584-object-oriented-tools-to-fit-plot-conics-and-quadrics.

45. Steger C. An unbiased detector of curvilinear structures. IEEE Transactions on pattern analysis and machine intelligence. 1998;20(2):113–125.

46. Wagner T, Hiner M, Raynaud X. thorstenwagner/ij-ridgedetection: Ridge Detection 1.4. 0. Detect ridges/lines with ImageJ: Ridge Detection. 2017;1(0).

47. Bahry E, Breimann L, Zouinkhi M, Epstein L, Kolyvanov K, Mamrak N, et al. RS-FISH: precise, interactive, fast, and scalable FISH spot detection. Nature Methods. 2022;19(12):1563–1567.

48. Thorndike RL. Who belongs in the family? Psychometrika. 1953;18(4):267–276.

49. Forouzesh E, Goel A, Mackenzie SA, Turner JA. In vivo extraction of Arabidopsis cell turgor pressure using nanoindentation in conjunction with finite element modeling. The Plant Journal. 2013;73(3):509–520.

50. Weber A, Braybrook S, Huflejt M, Mosca G, Routier-Kierzkowska AL, Smith RS. Measuring the mechanical properties of plant cells by combining micro-indentation with osmotic treatments. Journal of experimental botany. 2015;66(11):3229–3241.

51. Martin A, Lang D, Hanke ST, Mueller SJ, Sarnighausen E, Vervliet-Scheebaum M, et al. Targeted gene knockouts reveal overlapping functions of the five Physcomitrella patens FtsZ isoforms in chloroplast division, chloroplast shaping, cell patterning, plant development, and gravity sensing. Molecular plant. 2009;2(6):1359–1372.

Supporting information

S1 Text. Supplemental text include **Section 1.1**: Experimental protocols and moss imaging, **Section 1.2**: Experiment noise estimation, **Section 1.3**: Triangle error analysis, and **Section 1.4**: Data integration.

S1 Fig. Defining local angle on the wall surface points and triangulation. A. Local angle of each cell wall outline point calculated using $\alpha = \cos^{-1}(\hat{n} \cdot \hat{z})$. **B.** Triangulation map of local angle. **C.** (Top) Example triangle with local angle range. (Bottom) Example mapping of data along the local angle. Each triangle is represented by a line showing its angle range, and then it is sorted into its bins (example bin in gray).

S2 Fig. Confirmation of chosen spacing size in curvature calculation. A. Mean curvature results at 5 different spacing levels shown. **B.** The corresponding probabilities of mean curvature at the 5 spacing levels. We have chosen the bolded yellow line, spacing = 3 pixels.

S3 Fig. Experimental caulonema and chloronema hyphoid parameter fitting. A. Caulonema fitting, best fit at $a = 4.1$. **B.** Chloronema fitting, best fit at $a = 5.7$. (Top) Score of fit versus the parameter a shown in the equation below. (Bottom) Best fit hyphoid curve shown in red on top of 6 experimental cell outlines (both sides of each cell outline are included).

S4 Fig. Effect of different μ_h gradients in relation to the K_h gradient Three gradient cases are studied: the ratio of the side to the tip are equal for both K_h and μ_h, μ_h is constant, and the relative ratio of K_h and μ_h is equal. **A.** The turgid cell shapes of the three cases are compared. Inset shows the K_h gradient. **B.** The respective μ_h gradients shown. **C.** The respective elastic stretch ratios for the three cases shown.

S5 Fig. Sphere-fitting method to measure synthetic caulonema and chloronema tip surface modulus. A. Sphere radius of the turgid (blue) and unturgid sphere fitting (red) versus the maximum degrees of the synthetic cell outline used to fit the sphere. The three gradient cases are shown for each cell type. Visual sphere fit result examples are shown in the inset. **B.** Corresponding modulus value calculated by $Y_{tip} = \frac{R_B}{2(R_B - R_A)/R_A}$ where R_A is the unturgid sphere radius and R_B is the turgid sphere radius. Insets on some graphs show re-focused view. Chloronema results are shown in **C.** and **D.**. Modulus values are non-dimensionalized.

S6 Fig. Chloronema no noise results and no noise inference of K_h using area change Inference results of **A.** constant, **B.** nonlinear, and **C.** linear gradients using the triangulation scheme on one synthetic chloronema cell. **D.** Last column shows the inference of K_h calculated with $\lambda_s \lambda_\theta$ and calculated with S_B/S_A on top. Values are non-dimensionalized ($\kappa_{s,\theta} = \bar{\kappa}_{s,\theta}\bar{L}$, $\sigma_{s,\theta} = \bar{\sigma}_{s,\theta}/\bar{P}\bar{L}$, $K_h = \bar{K}_h/\bar{P}\bar{L}$).

S7 Fig. Triangulation size analysis with no noise. A. Representative triangulation on a synthetic caulonema cell and histogram of normalized triangle areas. Dashed line on histogram represents mean area displayed above to define each triangulation size: $\bar{\Delta}_A/\bar{L}^2$. **B.** Corresponding elastic stretch results from the three different triangulations. **C.** Corresponding tension results from the three different triangulations. **D.** Corresponding bulk modulus results from the three different

triangulations. The average relative error (ε_K) of the inference is shown. Values are non-dimensionalized ($\sigma_{s,\theta} = \bar{\sigma}_{s,\theta}/\bar{P}\bar{L}$, $K_h = \bar{K}_h/\bar{P}\bar{L}$).

S8 Fig. Low noise caulonema trial analysis. Average relative error of the bulk modulus inference for **A.** constant, **B.** nonlinear, and **C.** linear gradients versus the number of trials for three triangulation cases. In each case, n trials are chosen from 100 total cells, and this is repeated 100 times to obtain the standard deviation and mean shown in each graph. The corresponding 100 cell rescaled bulk modulus inferences are shown in each inset on top of the ground truth bulk modulus in magenta. Additionally, the knee of the curve is plotted along the mean, with its averaged error ($\bar{\varepsilon}_K$) at that trial number.

S9 Fig. Medium noise caulonema trial analysis. Average relative error of the bulk modulus inference for **A.** constant, **B.** nonlinear, and **C.** linear gradients versus the number of trials for three triangulation cases. In each case, n trials are chosen from 100 total cells, and this is repeated 100 times to obtain the standard deviation and mean shown in each graph. The corresponding 100 cell rescaled bulk modulus inferences are shown in each inset on top of the ground truth bulk modulus in magenta. Additionally, the knee of the curve is plotted along the mean, with its averaged error ($\bar{\varepsilon}_K$) at that trial number.

S10 Fig. High noise caulonema trial analysis. Average relative error of the bulk modulus inference for **A.** constant, **B.** nonlinear, and **C.** linear gradients versus the number of trials for three triangulation cases. In each case, n trials are chosen from 100 total cells, and this is repeated 100 times to obtain the standard deviation and mean shown in each graph. The corresponding 100 cell rescaled bulk modulus inferences are shown in each inset on top of the ground truth bulk modulus in magenta. Additionally, the knee of the curve is plotted along the mean, with its averaged error ($\bar{\varepsilon}_K$) at that trial number.

S11 Fig. High noise (two triangulation) caulonema trial analysis. Average relative error of the bulk modulus inference for **A.** constant, **B.** nonlinear, and **C.** linear gradients versus the number of trials for three triangulation cases. In each case, n trials are chosen from 100 total cells (with two triangulations each S1 Text), and this is repeated 100 times to obtain the standard deviation and mean shown in each graph. The corresponding 100 cell rescaled bulk modulus inferences are shown in each inset on top of the ground truth bulk modulus in magenta. Additionally, the knee of the curve is plotted along the mean, with its averaged error ($\bar{\varepsilon}_K$) at that trial number.

S12 Fig. High noise (two triangulation) chloronema trial analysis. Average relative error of the bulk modulus inference for **A.** constant, **B.** nonlinear, and **C.** linear gradients versus the number of trials for three triangulation cases. In each case, n trials are chosen from 100 total cells (with two triangulations each, see S1 Text), and this is repeated 100 times to obtain the standard deviation and mean shown in each graph. The corresponding 100 cell rescaled bulk modulus inferences are shown in each inset on top of the ground truth bulk modulus in magenta. Additionally, the knee of the curve is plotted along the mean, with its averaged error ($\bar{\varepsilon}_K$) at that trial number.

S1 Movie. Range of caulonema and chloronema cell outlines. Turgid cell outlines for all included caulonema and chloronema cells. Gradient value shows non-dimensionalized K_h side to tip.

S2 Movie. Range of caulonema and chloronema elastic stretch ratios and area stretch. Circumferential and meridional stretch ratios for all included caulonema and chloronema cells. Their multiplication, the area stretch, is also shown below. Gradient value shows non-dimensionalized K_h side to tip.

S13 Fig. Inferred endpoint ratio results across different triangulation sizes and noise levels from a synthetic chloronema cell. Contour map depicts the inferred endpoint ratio levels (K_{side}/K_{tip}) across a range of K_{side} and K_{tip} values at the three triangulation sizes and different noise levels: **A.** low noise, **B.** medium noise, and **C.** high noise. Results come from repeating the averaging of the standardized 10 cells to remove random effects (see S1 Text). Modulus values are non-dimensionalized ($K_h = \bar{K}_h/\bar{P}\bar{L}$).

S14 Fig. Two error quantifications for caulonema and chloronema cell bulk modulus inference with low noise Averaged error ($\bar{\varepsilon}_K$) for **A.** caulonema and **B.** chloronema cells. Relative absolute value endpoint ratio error $\bar{\varepsilon}_{K_{side}/K_{tip}}$) for **C.** caulonema and **D.** chloronema cells. In all parts, the underlying contours from Fig 7 (caulonema) and Fig S13 Fig (chloronema) are shown. The white dashed line denotes the boundary of 20% error and the white dotted line denotes the boundary of 5% error. Results come from repeating the averaging of the standardized 10 cells to remove random effects (see S1 Text). Modulus values are non-dimensionalized ($K_h = \bar{K}_h/\bar{P}\bar{L}$).

S15 Fig. Two error quantifications for caulonema and chloronema cell bulk modulus inference with medium noise Averaged error ($\bar{\varepsilon}_K$) for **A.** caulonema and **B.** chloronema cells. Relative absolute value endpoint ratio error ($\bar{\varepsilon}_{K_{side}/K_{tip}}$) for **C.** caulonema and **D.** chloronema cells. In all parts, the underlying contours from Fig 7 (caulonema) and Fig S13 Fig (chloronema) are shown. The white dashed line denotes the boundary of 20% error and the white dotted line denotes the boundary of 5% error. Results come from repeating the averaging of the standardized 10 cells to remove random effects (see S1 Text). Modulus values are non-dimensionalized ($K_h = \bar{K}_h/\bar{P}\bar{L}$).